

Mid-infrared interferometry of the massive young stellar object NGC 2264 IRS 1[★]

R. Grellmann¹, Th. Ratzka¹, S. Kraus², H. Linz³, Th. Preibisch¹, and G. Weigelt⁴

¹ Universitäts-Sternwarte, Ludwig-Maximilians-Universität München, Scheinerstr. 1, 81679 München, Germany

² University of Michigan, Department of Astronomy, Ann Arbor, MI 48109-1090, USA

³ Max-Planck-Institut für Astronomie, Königstuhl 17, 69117 Heidelberg, Germany

⁴ Max-Planck-Institut für Radioastronomie, Auf dem Hügel 69, 53121 Bonn, Germany

Received / Accepted

ABSTRACT

Context. The optically invisible infrared-source NGC 2264 IRS 1 lying north of the Cone Nebula is thought to be a massive young stellar object ($\sim 10 M_{\odot}$). Although strong infrared excess clearly shows that the central object is surrounded by large amounts of circumstellar material, no information about the spatial distribution of this circumstellar material has been available until now.

Aims. We used the ESO Very Large Telescope Interferometer to perform long-baseline interferometric observations of NGC 2264 IRS 1 in the mid-infrared regime. Our observations resolve the circumstellar material around NGC 2264 IRS 1, provide the first direct measurement of the angular size of the mid-infrared emission, and yield direct constraints on the spatial distribution of the dust.

Methods. We analyze the spectrally dispersed interferometric data taken with MIDI at two different position angles and baseline lengths. We use different approaches (a geometrical model, a temperature-gradient model, and radiative transfer models) to jointly model the observed interferometric visibilities and the spectral energy distribution.

Results. The derived visibility values between ~ 0.02 and ~ 0.3 show that the mid-infrared emission is clearly resolved. The characteristic size of the MIR-emission region is $\sim 30 - 60$ AU; this value is typical for other YSOs with similar or somewhat lower luminosities. A comparison of the sizes for the two position angles shows a significant elongation of the dust distribution. Simple spherical envelope models are therefore inconsistent with the data. The radiative transfer modeling of our data suggests that we observe a geometrically thin and optically thick circumstellar disk with a mass of about $0.1 M_{\odot}$.

Conclusions. Our modeling indicates that NGC 2264 IRS 1 is surrounded by a flat circumstellar disk that has properties similar to disks typically found around lower-mass young stellar objects. This result supports the assumption that massive young stellar objects form via accretion from circumstellar disks.

Key words. techniques: interferometric - stars: individual: NGC 2264 IRS 1 - stars: formation-stars: circumstellar matter

1. Introduction

The question of how massive stars ($> 8 M_{\odot}$) form still remains unclear because observations of massive young stellar objects (MYSOs) are rare (Zinnecker & Yorke 2007). This has several reasons. First of all, these objects are surrounded by large amounts of gas and dust, which absorb nearly all the optical and near-infrared (NIR) radiation from the central source, thus making a direct observation very difficult. Second, their large distances mean that to study them we need data of high angular resolution. Other difficulties are the fast evolution of MYSOs and that they are rarely found in isolation.

Two different formation scenarios for MYSOs are currently discussed: the coalescence scenario and a formation similar to low mass protostars. In the first scenario, several low mass stars merge and finally form a single, more massive star (Bonnell et al. 1998; Zinnecker & Bate 2002). In the second scenario, the radiation pressure problem that would prevent spherical accretion as soon as the protostellar mass exceeds $\sim 10 M_{\odot}$ is solved by stellar outflows, which open a cavity in polar direction, through which the radiation can escape and the radiation

pressure in the equatorial plane is lowered. Therefore, an infall of material in this plane is possible. Observations have provided some evidence that massive stars can form in an analogous way to low mass stars. For instance, circumstellar disks (e.g., IRAS 20126+4104, Cesaroni et al. 2005; AFGL 490, Schreyer et al. 2006; IRAS 13481-6124, Kraus et al. 2010), molecular outflows, or collimated jets (e.g., Cunningham et al. 2009) are often interpreted as evidence of ongoing accretion. From the theoretical side, both the competitive accretion (Bonnell & Bate 2006) and the turbulent core model (McKee & Tan 2003) agree with the formation of disks. Furthermore, simulations demonstrate that high-mass stars may form by disk accretion (Kuiper et al. 2010).

Traditionally, the spatial distribution of the surrounding dust was usually studied by the modeling the spectral energy distribution (hereafter SED). Such SED model fits are highly ambiguous (Thamm et al. 1994; Men'schikov & Henning 1997). Therefore, more information is required to determine the real geometry of the circumstellar material. To test the existence of a circumstellar disk, and thus the disk accretion scenario of massive star formation, information at high angular resolution (corresponding to physical scales below 100 AU) is needed. Furthermore, only radiation at long wavelengths (e.g., infrared, sub-mm) is able to escape from the dense dusty surroundings of

* Based on observations collected at the European Organisation for Astronomical Research in the Southern Hemisphere, Chile, observing programs 076.C-0725(B) and 082.C-899(A).

the star. Infrared long-baseline interferometry can thus provide direct spatial information on the required small scales.

NGC 2264 is a young, star-forming cluster with an age of about 3 Myr located in the Mon OB 1 molecular cloud complex. Literature values for the distance of the cluster vary between 400 pc and 1000 pc, although here we adopt the most recent value of 913 pc (Baxter et al. 2009). NGC 2264 IRS 1, the brightest IR-source in this region, was discovered in 1972 by D. Allen (hence is also called Allen's Source) and has no optical counterpart. Allen (1972) pointed out that since NGC 2264 IRS 1 is the brightest and most luminous source in this field, it is the likely source of the radiation pressure creating the Cone Nebula. It is believed to be a young star with a mass of $9.5 M_{\odot}$, spectral type B0-B2 (Thompson et al. 1998), a luminosity of $3.5 \cdot 10^3 L_{\odot}$ (Harvey et al. 1977), and a visual extinction of 20-30 mag. However, owing to its high extinction in the optical, all values are rather uncertain and should be interpreted with care, e.g., luminosity values between $2.3 \cdot 10^3 L_{\odot}$ (Nakano et al. 2003) and $4.7 \cdot 10^3 L_{\odot}$ (Schwartz et al. 1985) can be found in the literature.

NGC 2264 IRS 1 is associated with molecular outflows and dense molecular clumps, and in near-infrared images a twisted jet-like feature can be seen extending north of the source (Schreyer et al. 1997; Ward-Thompson et al. 2000). The morphology of the circumstellar environment is unclear. Several studies did not find any hint of an asymmetric structure. Schreyer et al. (2003) were unable to detect any signs of a circumstellar disk in their molecular line study and de Wit et al. (2009) do not discern any disk-like structure in their images taken in the MIR with COMICS. However, models of a spherical symmetric distribution of the circumstellar material fail to reproduce the SED of the object in its entirety and were ruled out in several publications (Thompson & Tokunaga 1978; Harvey et al. 1977). However, the spatial resolution of all these studies may not be sufficient to resolve a disk-like structure.

In this paper, we present mid-infrared interferometric observations of the MYSO NGC 2264 IRS 1 performed with the Mid-Infrared Interferometric Instrument (MIDI) at the Very Large Telescope Interferometer (VLTI). The MIDI data and their reduction are shown in Sect. 2. Different modeling approaches (geometrical, temperature-gradient, and radiative transfer models) for the visibilities and the SED are presented in Sect. 3. Implications for the object and final conclusions are discussed in Sect. 4.

2. Observations and data reduction

NGC 2264 IRS 1 was observed on 2005 December 23 in the course of ESO observing programme 076.C-0725(B) (PI: S. Kraus) and on 2009 February 15 in the course of ESO programme 082.C-0899(A) (PI: M. Feldt) with MIDI at the VLTI (see Table 2). MIDI (Leinert et al. 2003) is a two-telescope beam-combiner working in the wavelength range from 8 to $13 \mu\text{m}$ and using the principle of a Michelson interferometer. To measure the fringe amplitude, the optical path difference (OPD) is varied with internal delay lines. The 2005 data of NGC 2264 IRS 1 were taken with a baseline of 89.1 m in the SCI-PHOT mode, in which interferometric and photometric data are measured simultaneously. The grism (a combination of a grating and a prism) with a spectral resolution of $\frac{\Delta\lambda}{\lambda} = 230$ was used. In the same night, two calibrators were observed with the same configuration. HD 39425 a few hours earlier and HD 61421 directly after the object. The 2009 data were taken with a baseline of 40.2 m in the HIGH-SENS mode, in which interferometric and photometric data are obtained separately. For this obser-

vation, the prism with a spectral resolution of $\frac{\Delta\lambda}{\lambda} = 30$ was used. HD 48217 and HD 49161 served as calibrators.

For data reduction and calibration, we used the software package MIA+EWS (Köhler & Jaffe 2008). With this software, the correlated flux, visibility, and the total flux can be determined. Typical errors in one single MIDI visibility measurement are about 10% (Leinert et al. 2004). As an estimate of the error bars, the standard deviation in the results for different calibrators was used. As the conditions during the observation in 2009 were not photometric, we did not use the 2009 photometry data, but the photometry from the 2005 measurement to obtain the visibility. Figure 1 (left) shows the calibrated visibilities for both observations.

Furthermore, a low-resolution IR spectrum of NGC 2264 IRS 1, measured with the SWS instrument aboard the ISO satellite is available (TDT No. 71602619, PI: D. Whittet), as well as fluxes in several other wavelength bands. These data points are listed in Table 1. Fig. 1 (right) shows the total flux spectrum of NGC 2264 IRS 1 as measured by MIDI in 2005 compared to the total flux spectrum measured by the ISO satellite. Both spectra display a deep absorption feature over the whole MIDI wavelength range caused by silicates. The shape of both spectra (MIDI and ISO) is similar but the flux level of the MIDI spectrum is about 25 Jy (about 20 %) lower, which might be due to the different beam sizes of the instruments (see Table 1). The spurious feature in the MIDI spectrum at wavelengths between $9.3 \mu\text{m}$ and $9.8 \mu\text{m}$ is due to atmospheric ozone. Several absorption features can be identified in the ISO spectrum (Gibb et al. 2004). The broad absorptions around 3.1 and $6.0 \mu\text{m}$ arise mainly from water ice, while the carrier of the $6.8 \mu\text{m}$ feature is more uncertain, but might be associated with solid NH_4^+ . A rather sharp feature at $4.27 \mu\text{m}$ is commonly attributed to CO_2 ice (Guertler et al. 1996), as is the absorption seen at $15.2 \mu\text{m}$. The feature around $4.7 \mu\text{m}$ is probably a combination of CO gas line absorption and a variety of ice absorption features. All these findings point to relatively large column densities of cold dense material along the line of sight towards the central source.

3. Modeling

We now attempt to derive the properties of NGC 2264 IRS 1 from our measurements using different modeling approaches. First, we use simple geometrical models to characterize the size of the dust emission region (see Sect. 3.1). To test for the possibility of a circumstellar disk, we compare the data with a temperature-gradient model for such a disk (Sect. 3.2). To check the parameter space over a wider range, we employ the on-line model SED fitter by Robitaille et al. (2007) in Sect. 3.3. A more detailed modeling is done in Sect. 3.4, where the two-dimensional radiative transfer code RADMC is used.

3.1. Simple geometrical models

As a first step, one can derive an estimate of the diameter of the mid-infrared (MIR) emission region of the object from the visibilities by using simple geometrical models. For more details of this we refer to Berger & Segransan (2007) and Tristram (2007).

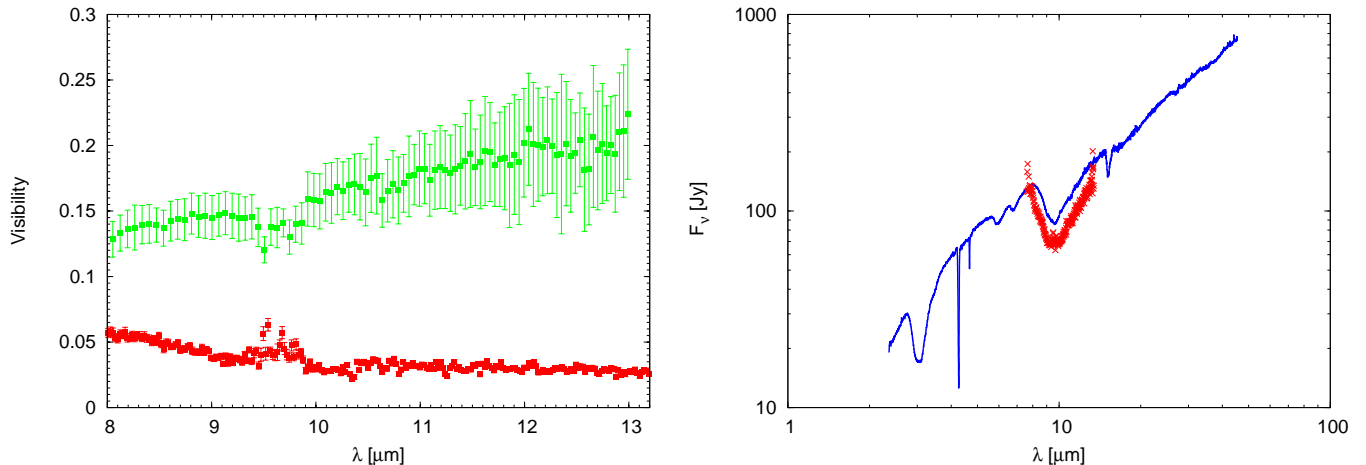
We first consider the possibility of a binary. Its existence would result in a sinusoidal variation in the visibility (versus wavelength), ranging between a maximum and a minimum value. The maximum value depends on the extension of the MIR emission regions (and would be 1 for point like sources),

Table 1. Measured fluxes for NGC 2264 IRS 1

Wavelength [μm]	Flux [Jy]	Instrument/Reference	Aperture
2-45	9.670	ISO (Sloan et al. (2003))	$14'' \times 20''$
1.65	0.9 ± 0.04	2-MASS	$4''$
2.2	6.8 ± 0.016	2-MASS	$4''$
8-13	60-130	MIDI	$0.5''$
12.0	146 ± 9	IRAS	$0.75' \times 4.5'$
24.5	330	COMICS	$42'' \times 32''$
25.0	324 ± 13	IRAS	$0.75' \times 4.6'$
53.0	980 ± 50	Harvey et al. (1977)	$17''$
60.0	911	IRAS	$1.5' \times 4.7'$
70.0	960 ± 290	Sargent et al. (1984)	$3'$
100.0	1560	IRAS	$3' \times 5'$
100.0	1645 ± 82	Harvey et al. (1977)	$28''$
175.0	1530 ± 77	Harvey et al. (1977)	$46''$
350.0	188 ± 70	Chini et al. (1986)	$30''$
1300	13 ± 2.5	Chini et al. (1986)	$90''$

Table 2. Observation log of the MIDI measurements of NGC 2264 IRS 1

Date	Proj. Baseline [m]	PA [$^{\circ}$]	Mode
12/23/2005	89.1 (UT2-UT4)	81.1	SCI-PHOT&GRISM
02/15/2009	40.2 (UT2-UT3)	43.9	HIGH-SENS&PRISM

**Fig. 1.** *Left:* Visibilities of NGC 2264 IRS 1 measured with MIDI. The visibility points measured in 2005 (projected baseline length 89.1 m) are shown in red, those measured in 2009 (projected baseline 40.2 m) are shown in green. *Right:* Spectrum of NGC 2264 IRS 1 as measured with MIDI (red crosses) in 2005 compared to the ISO spectrum (blue line).

whereas the amplitude depends on the flux ratio of both components (the minimum would be 0 for a flux ratio of 1:1). Owing to the slit width of MIDI (see Table 1), the maximum separation of a binary that can be identified with this instrument is ~ 230 AU. The minimum separation at which a binary could be resolved with the 90 m baseline is ~ 30 AU (diffraction limit; half a period of the modulation in the visibility would be seen). Both observed visibilities show no typical sinusoidal variation, hence a binary system with a separation of > 30 AU is unlikely and not considered during the modeling process. However, with our measurements we could miss very faint binary companions or systems with separations of about 30 AU oriented non-parallel to the position angle of the 90 m baseline.

We consider two different geometrical models for a single source: a Gaussian distribution and a uniform disk (UD). The results can be seen in Fig. 2. All curves show an increasing size

of the object with increasing wavelength, as expected because of the different dust temperatures in different parts of the dust distribution. For the measurement performed with the 90 m baseline, the size varies between 16 and 30 mas for the Gaussian model and between 20 and 35 mas for the uniform disk model, whereas for the 40 m baseline, the size of the object lies between 30 and 44 mas for the Gaussian model and between 44 and 64 mas for the uniform disk model. As the observations were taken at different position angles, the different size estimations suggest an elongation in the dust distribution (e.g., a circumstellar disk or a flattened envelope). Although the intensity profile of the real source possibly differs from those distributions, the Gaussian model in particular is usually a good approximation of the mid-infrared morphology of YSOs. Despite all the uncertainties in the visibility measurements, hence the size estimation, the fitting of the Gaussian model still helps us identify an asymmetry with

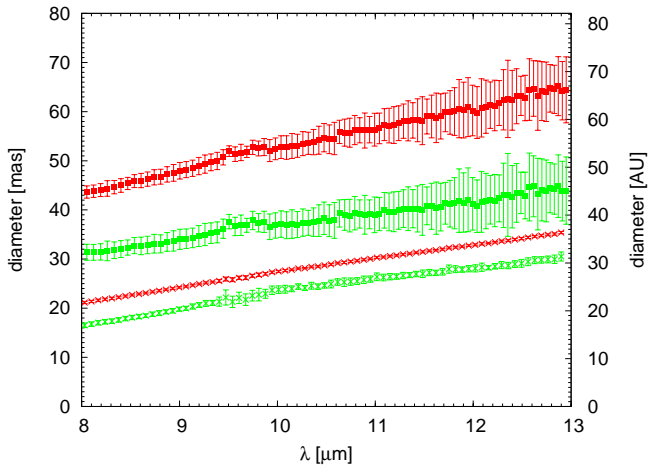


Fig. 2. Mid-infrared diameter of NGC 2264 IRS 1 as a function of wavelength for the 2005 data (crosses) measured with a 90 m baseline and the 2009 data (rectangulars) measured with a 40 m baseline. The values for the diameter in AU (right y-axis) were computed using a distance of 913 pc. Two different models were used: a Gaussian model (red) and a uniform disk model (green).

a significance of 3σ and the UD model within 2σ . This result clearly suggests that the MIR emission region is not spherically symmetric but elongated.

3.2. Temperature gradient model

Many young stars of both low and high mass are known to have circumstellar disks (e.g., Kraus et al. 2010; Leinert et al. 2004; Ratzka et al. 2009). As a first approach to interpreting simultaneously SED and N-band spatial data, we therefore use a temperature-gradient model for a circumstellar disk as described in Malbet et al. (2005). The disk specified by this model is optically thick, but geometrical thin with an inner radius r_{\min} and an outer radius r_{\max} . The distribution of the temperature in the disk is described following the equation

$$T(r) = T_0 \left(\frac{r}{r_0} \right)^{-q}, \quad (1)$$

where T_0 is the temperature at a reference radius $r_0 = 1$ AU. The exponent q is expected to lie approximately between 0.5 for passive, irradiated, flared disks and 0.75 for passive, irradiated, flat disks (Malbet et al. 2005).

One can imagine such a disk to be composed of rings with radius r and thickness dr . If every ring emits blackbody radiation, one can evaluate the flux by integrating over the radius r such that

$$F_\lambda(0) = \frac{2\pi}{d^2} \int_{r_{\min}}^{r_{\max}} r B_\lambda(T(r)) \cos(i) dr, \quad (2)$$

where d is the distance to the object, B_λ the Planck function for a blackbody with temperature $T(r)$, and i the inclination of the disk. For the visibility, one then gets

$$V_\lambda(b, 0) = \frac{2\pi}{F_\lambda(0)d^2} \int_{r_{\min}}^{r_{\max}} r B_\lambda(T(r)) J_0\left(2\pi b \frac{r}{d}\right) dr, \quad (3)$$

where J_0 is the Bessel function of zeroth order and b the baseline according to

$$b = \sqrt{u_\Theta^2 + v_\Theta^2 \cdot \cos^2(i)}.$$

Here, Θ is the position angle of the disk and u_Θ and v_Θ are given by

$$u_\Theta = u \cos \Theta - v \sin \Theta$$

and

$$v_\Theta = u \sin \Theta + v \cos \Theta.$$

We calculated a large number (≈ 1000) of temperature-gradient models and tried to find a model that is simultaneously able to reproduce all observations (both visibilities and SED). For this, we varied the inner radius between 0.5 and 2 AU (in steps of 0.5 AU) and T_0 between 1400 and 3000 K in steps of 200 K. For the parameter q , we tested the values 0.5, 0.6, and 0.7. Inclination and position angle were varied in steps of 10° .

The temperature gradient model with the parameters listed below is able to reproduce the SED in the mid- and far-infrared, but fails in the near-infrared. All of the calculated models failed completely to reproduce the shape of the visibility measured with the 40 m baseline (rising values going to larger wavelengths). As the best-fit model, we therefore show the model that most successfully reproduces the other visibility curve and the SED simultaneously, although different models led to a better fit for the 40 m visibility at least with respect to its absolute level. The best-fit model is shown in Fig. 3 and has the following parameters:

- $r_{\min} = 0.5$ AU
- $r_{\max} = 4000$ AU
- $T_0 = 2350$ K
- $i = 75^\circ$
- $q = 0.5$
- $\Theta = 90^\circ$

The spectral features seen in the SED and the effects of the silicate absorption on the visibility cannot be reproduced, as radiative transfer effects (emission, absorption, and scattering) are not included in the model.

A temperature of $T_0 = 2350$ K at a reference radius of 1 AU would imply a temperature of 3250 K at the inner disk radius of 0.5 AU for this model. This is much too hot for the existence of normal dust grains. A possible explanation could be the existence of an inner gas disk (Kraus et al. 2008) or of dust grains with higher sublimation temperature (Benisty et al. 2010).

3.3. Disk and envelope models in the Robitaille grid

To check a wider parameter space for different models (especially for the possibility of a circumstellar envelope), we employed the online SED fitting tool developed by Robitaille et al. (2007). This tool compares 200,000 models of the SEDs of YSOs, which were precomputed using a 2D radiative transfer code (Whitney et al. 2003), with the measurements. These models are described by a set of 28 parameters, such as the properties of the central object (e.g., mass, temperature), the properties of the circumstellar envelope (e.g., outer radius, accretion rate, opening angle), the circumstellar disk (e.g., mass, outer disk radius, flaring), and the ambient density (for details see Robitaille et al. 2006). In addition to defining SED points, the user has to set a range for the interstellar extinction and for the distance of the object. We chose the interstellar extinction A_V to be between 0 and 40 mag and the distance d to be between 800 pc and 1000 pc.

The number of points that can be fitted by the SED online tool is limited. Therefore, from the ISO spectrum about one flux

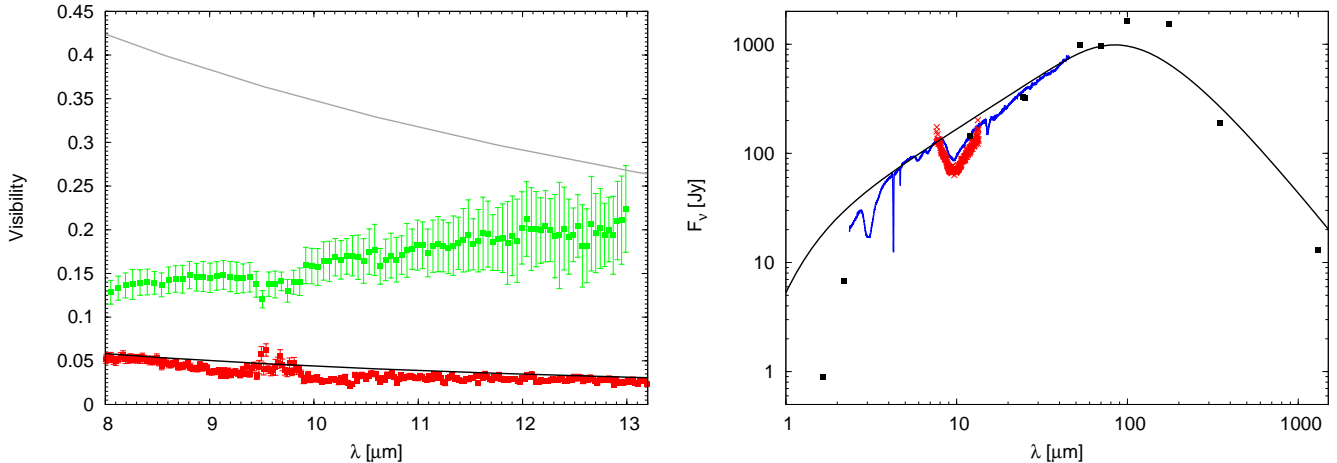


Fig. 3. *Left:* Comparison of the best-fit temperature-gradient model to the visibilities of NGC 2264 IRS 1 with the model parameters described in Sect. 3.2 (green for the 40 m baseline, red for the 90 m baseline). The resulting modeled visibility for the 40 m baseline is shown by the gray line, the one for the 90 m baseline by the black line. *Right:* Comparison of the SED of our best-fit temperature-gradient model (black) described in Sect. 3.2 with the ISO spectrum (blue) of NGC 2264 IRS 1. The MIDI spectrum is shown with red crosses, all other measurements from Table 1 are shown with black rectangulare.

point per one micron was used. From the MIDI spectrum, about two flux points per micron were chosen as the shape of the spectrum changes much more in this wavelength regime because of the silicate absorption feature.

When comparing the model visibilities and fluxes to the observed data, it is important to consider the very different (effective) beam-sizes of the different observations. The MIDI instrument has an effective field-of-view of $0.5''$ (slit width), corresponding to ≈ 450 AU at the distance of our target. The beam sizes for all other data points beyond near-infrared wavelengths are much larger: the beam size from which the ISO spectrum was extracted ($\approx 13\,000 \times 18\,000$ AU) is already ≈ 1100 times larger, and the beam sizes for all far-infrared data points are at least ~ 3000 times larger than the MIDI field-of-view. The ISO and far-infrared fluxes do therefore not only trace the emission from the central YSO and its immediate circumstellar material (on spatial scales of up to ~ 500 AU), but also contain contributions from the surrounding extended molecular cloud, on spatial scales of $\gtrsim 20\,000$ AU ($\gtrsim 0.1$ pc).

Therefore, as a first approach we include all SED points with $\lambda > 13\,\mu\text{m}$ only as upper limits. To compute the visibilities, we used the HO-CHUNK code from Whitney et al. (2003) to calculate images for the model. Doing so, the ten best-fit models consist of circumstellar disks only (see Sect. 3.3.1). As a second approach, none of the data points was used as an upper limit, but they all were given with their errors. Here, rather different best-fit models are found by the fitting tool. They all consist of a large circumstellar envelope and either have no additional disk, or just a small ring-like structure with radii from 0.5 to 8 AU (see Sect. 3.3.2). For similar applications of this fitting tool and its advantages and limitations in this respect, we refer to for instance Linz et al. (2009), de Wit et al. (2010), and Follert et al. (2010). We note that the parameter space is not covered uniformly. In particular, the spacing of the grid parameters is much finer in the case of low-mass YSOs than for MYSOs.

3.3.1. Robitaille disk models

The SED and visibilities of the best-fit Robitaille disk models are shown in Fig. 4. This model is able to reproduce the flux in

the near- and mid-infrared. To reproduce the flux in the FIR, one would have to add for example some blackbody components as shown later for the RADMC model (see Sect. 3.4). The model can reproduce the level of the 90 m baseline visibility, and also the 40 m baseline visibility is reproduced within the errorbars. The parameters of this best-fit model are (model ID 3004478):

- $M_{\star} = 11.6 M_\odot$
- $T_{\star} = 27,720$ K
- $L_{\star} = 1.21 \times 10^4 L_\odot$
- $r_{\text{out}} = 84$ AU
- $h_{\text{disk}}(100 \text{ AU}) = 5.6$ AU
- $m_{\text{disk}} = 0.09 M_\odot$
- $i = 70^\circ$
- $A_V = 20.27$ mag
- $\Theta = 40^\circ$

Here, r_{out} is the outer disk radius and h_{disk} would be the height of the disk when extending it to a radius of 100 AU.

3.3.2. Envelope plus disk models

The Robitaille envelope model with the smallest χ^2 is shown in Fig. 5. It fails to model especially the shape of the 40 m baseline visibility curve. The flux in the mid-IR can be reproduced, but the model cannot reproduce the flux in the near-IR. To attain the flux level in the far-IR, one would once again have to add, e.g., a blackbody component. The parameters of the best-fit model are (model ID 3019090):

- $M_{\star} = 8.5 M_\odot$
- $T_{\star} = 4200$ K
- $R_{\star} = 82 R_\odot$
- $L_{\star} = 2.05 \times 10^3 L_\odot$
- $r_{\text{envelope}} = 36,000$ AU
- $m_{\text{envelope}} = 1.84 M_\odot$
- $r_{\text{disk}} = 3.6$ AU
- $h_{\text{disk}}(100 \text{ AU}) = 7.7$ AU
- $m_{\text{disk}} = 0.2 M_\odot$
- $i = 18^\circ$
- $A_V = 3.8$ mag.

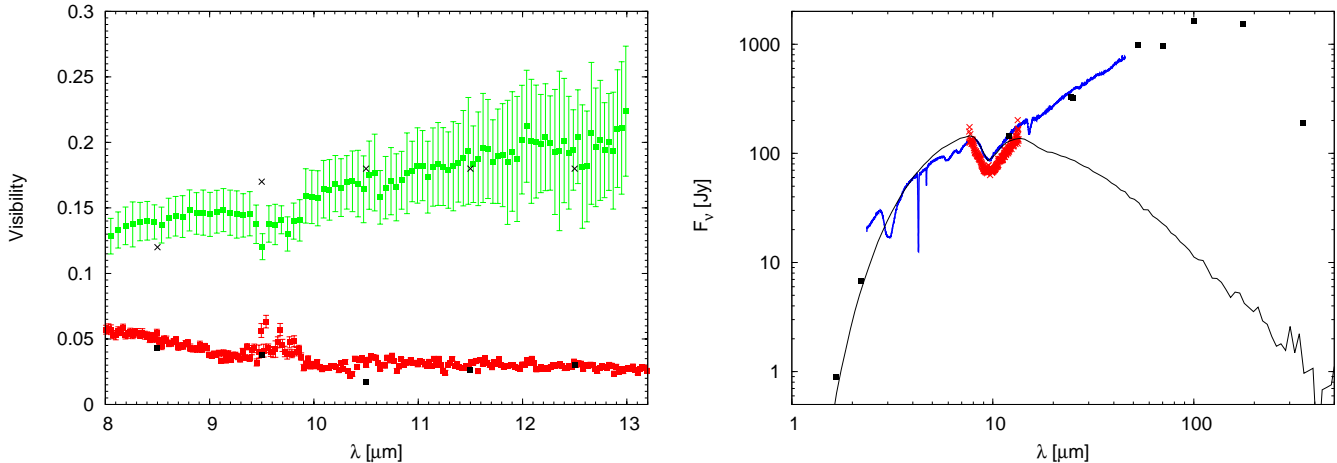


Fig. 4. *Left:* Comparison of the best-fit Robitaille disk model (black crosses 40 m baseline, black rectangles 90 m baseline) for the visibilities of NGC 2264 IRS 1 with the MIDI visibilities (red 90 m baseline, green 40 m baseline). *Right:* Comparison of the best-fit Robitaille model (black) for the spectrum of NGC 2264 IRS 1 with the ISO spectrum (blue), the MIDI spectrum (red crosses), and the data points from Table 1 (black rectangles).

A change in the position angle does not in this case lead to significant differences for this model, as the dust distribution is nearly symmetric. Therefore, a best-fit position angle cannot be given. As mentioned before, this model consists mainly of a circumstellar envelope, with an outer radius of r_{envelope} . However, there is also a disk component with a very small outer radius $r_{\text{disk}} = 3.6 \text{ AU}$. The central object is much cooler and larger than the central object in the disk models.

3.4. Two-dimensional radiative transfer modeling

A more detailed physical model for a circumstellar disk is obtained by using the two-dimensional (2-D) radiative transfer model code RADMC (Version 3.1, Dullemond & Dominik 2004), which provides calculations of continuum radiative transfer in three-dimensional axisymmetric (therefore 2-D) circumstellar dust distributions around a central illuminating star. The main radiative transfer calculations are done with a Monte Carlo algorithm. To produce spectra and images, a post-processing with a ray-tracing code is done. The disk is described using a passive irradiated flared disk based on the model of Chiang & Goldreich (1997), but the code also allows the user to insert a vertical puffed-up inner rim to produce a self-shadowed disk. The space is mapped in spherical coordinates. We therefore have radial grid points r and angular grid points θ , where $\theta = 0$ is the polar axis and $\theta = \theta_{\max} = \frac{\pi}{2}$ is the equatorial plane. We again tried to reproduce the SED and visibilities simultaneously and also to fit the silicate absorption feature. To scan the parameter space, more than 10,000 different models were calculated and compared to the observed data.

The geometry of the disk is described by the pressure scale height h_{disk} at a reference radius r_{disk} , and an exponent p in the following way (for $r_{\text{in}} < r < r_{\text{disk}}$):

$$h(r) = h_{\text{disk}} \cdot \left(\frac{r}{r_{\text{disk}}} \right)^p. \quad (4)$$

Furthermore, either the surface density at the outer radius σ_0 can be given by the user directly, or (as we did) be calculated from the user-defined total disk mass $m_{\text{disk}} = m_{\text{gas}} + m_{\text{dust}}$. We used

a gas-to-dust ratio of 100. The surface density as a function of radius is then given by

$$\sigma(r) = \sigma_0 \cdot \left(\frac{r}{r_{\text{disk}}} \right)^{-q}. \quad (5)$$

For $r > r_{\text{disk}}$, the exponent q is chosen to be equal to 12 such that the density drops so fast that r_{disk} is effectively the outer disk radius. This outer radius was varied between 30 AU and 150 AU. The density distribution in the whole disk is described by

$$\rho(r, \theta) \propto \frac{\sigma(r)}{h(r) \cdot r} \cdot \exp \left[-\frac{1}{2} \left(\frac{\theta_{\max} - \theta}{h(r)} \right)^2 \right]. \quad (6)$$

Parameters that remained fixed during the modeling process, were the temperature of the central object $T_{\text{star}} = 25,000 \text{ K}$ (according to the spectral type B0-B2), the exponent $q = 12$ for $r > r_{\text{disk}}$, and the temperature at the inner rim $T_{\text{in}} = 1700 \text{ K}$. For the chemical composition of the dust, the optical properties of astronomical silicate (Draine & Lee 1984) and graphite were chosen, using the grain size distribution of the MRN model (Mathis et al. 1977). A mixture of 70% silicate and 30% graphite was assumed.

In addition to the original RADMC code, we introduced foreground extinction A_V , as otherwise all models failed to reproduce the deep silicate absorption feature. Parameters that were varied during the fitting process are shown in the following list together with their values for the best-fit RADMC model:

- $r_{\text{disk}} = 50 \text{ AU}$
- $h_{\text{disk}} = 0.1$
- $L_{\text{star}} = 3.98 \times 10^3 L_{\odot}$
- $p = 2/7$
- $m_{\text{disk}} = 0.1 M_{\odot}$
- $q = 2.5$ for $r < r_{\text{disk}}$
- $i = 30^\circ$
- $\text{PA} = 40^\circ$
- $A_V = 27 \text{ mag.}$

This best-fit model is shown in Fig. 6. It provides a good fit to the visibilities as well as the SED up to $12 \mu\text{m}$.

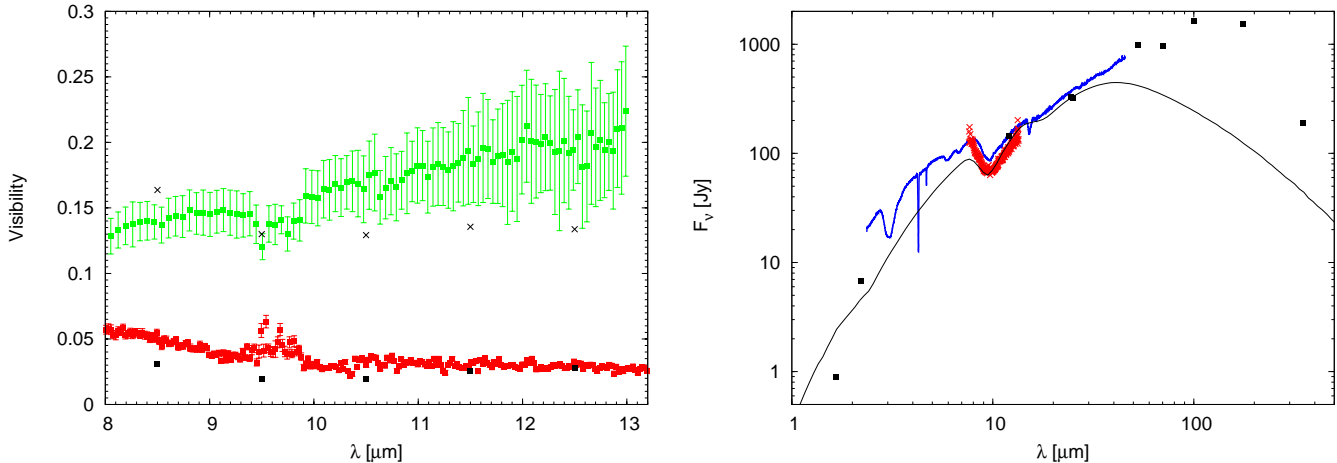


Fig. 5. *Left:* Comparison of the best-fit Robitaille envelope model (black crosses 40 m baseline, black rectangles 90 m baseline) for the visibilities of NGC 2264 IRS 1 with the MIDI visibilities (red 90 m baseline, green 40 m baseline). *Right:* Comparison of the best-fit Robitaille model (black) for the spectrum of NGC 2264 IRS 1 with the ISO spectrum (blue), the MIDI spectrum (red crosses), and the data points from Table 1 (black rectangles).

The RADMC model describes the central YSO and its circumstellar matter up to the outer disk radius of 50 AU, i.e. predicts the emission in the central 100 AU diameter region. Since this area is completely inside the MIDI field-of-view, the model visibility can be directly compared to the observed visibilities. For the fits to the SED, however, we have to take into account that the very large beams of the far-infrared observations must clearly include emission from the surrounding large-scale cloud, on spatial scales of $\sim 20\,000$ AU (~ 0.1 pc) and larger, which is far outside the $r = 50$ AU model area. This large-scale cloud emission should not be confused with a possible circumstellar envelope, but represents the molecular clump and the surrounding cloud in which IRS 1 is embedded (see discussion below). The mm-maps presented by Schreyer et al. (1997) show that the size of this cloud is about 1' (corresponding to $\sim 55\,000$ AU or ~ 0.27 pc).

The effects of this large-scale cloud are as follows: our MIDI measurements are insensitive to this large-scale emission, because it is far more extended than the angular resolution (and also the field-of-view) of MIDI. Since the large-scale cloud emission is completely over-resolved for MIDI, it will not affect the observed visibilities. The observed fluxes, however, are expected to be strongly affected by the large-scale cloud. First, the cloud material in front of the embedded object IRS 1 will cause considerable extinction. This effect is represented by the foreground extinction we use in our modeling. The second effect is that the cool dust in the large-scale cloud will produce far-infrared and mm-emission. Owing to the large beam sizes of the far-infrared and mm-observations, a large fraction of the observed fluxes in these beams will result from the large-scale cloud, and not from the central embedded object IRS 1. This explains why our RADMC model fluxes at wavelengths $\gtrsim 20\,\mu\text{m}$ are considerably lower than the observed fluxes. To approximately include this large-scale cloud emission component in our model, we added to our SED model in Fig. 6 two additional blackbody components. For the temperature of the first component, we used $T = 55$ K, as determined by Schreyer et al. (1997) for the clump in which IRS 1 is embedded. For the second component, we used a temperature of 120 K, which is typical of warm dust around massive YSOs in so-called “hot-cores” (Herbst & van Dishoeck 2009). Fig 6 shows that with the addition

of these two components good agreement between the observed fluxes and the model can be achieved.

An interesting question is whether this 120 K component could be considered as an envelope around the disk, as for one interpretation of hot cores as an infalling envelope undergoing an intense accretion phase (Osorio et al. 2009). The RADMC model of a disk without surrounding envelope provides a very good fit of both visibilities. Adding a spherical circumstellar envelope with a radius of ≤ 250 AU would change the model visibilities significantly (by $> 5\%$) and lead to disagreement between the model and the data. On the other hand, a (more or less) homogeneous envelope with a radius of > 250 AU would be over-resolved for MIDI and not affect the visibilities. However, to reproduce the far-infrared fluxes in the SED, the radius of the 120 K emitting region has to be at least ≥ 400 AU (in the limiting case of optically thick blackbody emission). Owing to the limited MIDI field of view, the difference between the ISO and the MIDI spectrum could result from such an extended structure. The question of whether an extended circumstellar envelope is present can thus not be answered by the available data. Whether the material in such a hypothetical envelope would be gravitationally bound and ultimately accrete onto the circumstellar disk, remains another open question.

4. Discussion

We now want to discuss our findings presented in Sect. 3. We first compare the size of the mid-IR emission region as calculated in Sect. 3.1 to the corresponding sizes of similar objects. We then discuss the radiative transfer models.

4.1. Comparison to MIR sizes of other massive YSOs

The near-IR sizes of the disks of most YSOs (in particular Herbig Ae stars) show a tight correlation with the luminosity (Monnier et al. 2005) because the emission in the NIR comes from regions close to the dust sublimation radius, which is sensitive to radiation from the central star and scales approximately with the square root of the luminosity. The mid-infrared emission, in contrast, originates from a wider range of regions: the hot inner wall located at the dust sublimation radius, the surface

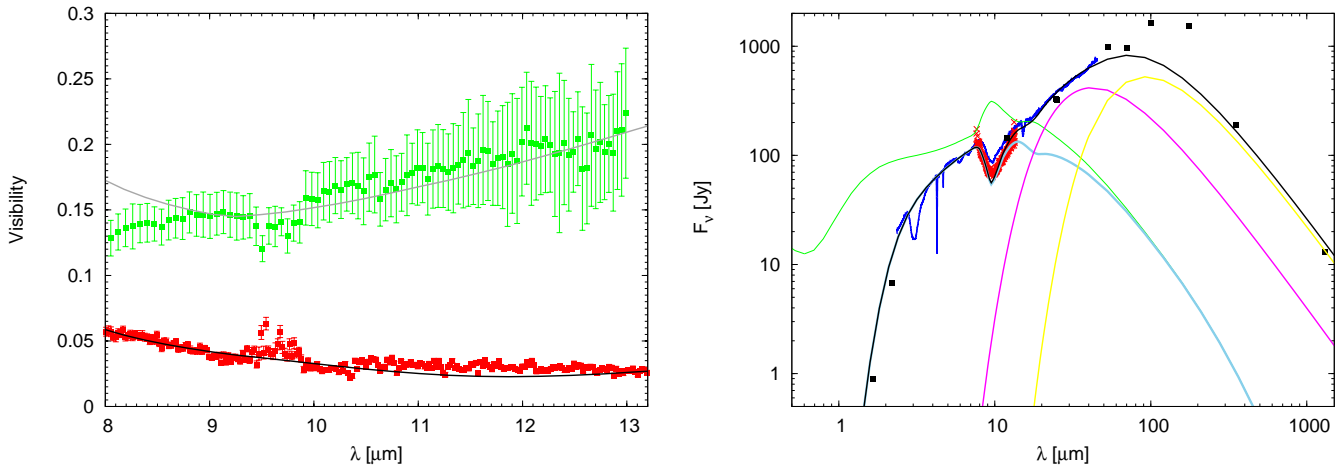


Fig. 6. *Left:* Comparison of the best-fit RADMC model (gray 40 m baseline, black 90 m baseline) for the visibilities of NGC 2264 IRS 1 with the MIDI visibilities (red 90 m baseline, green 40 m baseline). *Right:* Comparison of the best-fit RADMC model for the spectrum of NGC 2264 IRS 1 with the ISO spectrum (blue), the MIDI spectrum (red crosses), and the data points from Table 1 (black rectangulare). The green line is the RADMC model without foreground extinction, the light blue line the model with a foreground extinction of 27 mag, and the black line the RADMC model with extinction and two additional blackbody components with temperatures of 55 K (yellow) and 120 K (pink).

of an irradiated disk, and the circumstellar envelope. As shown in Monnier et al. (2009), the size of the region emitting in the MIR therefore spans a much larger region for a given luminosity. For circumstellar disks, factors such as the flaring of the disk and the shadowing caused by the inner rim play an important role. Here, we wish to compare the MIR size of NGC 2264 IRS 1 as found for the uniform disk model with the MIR sizes of other MYSOs, as well as with those of Herbig Be stars.

Only a few other MYSOs have been studied with high angular resolution in the MIR until now. Amongst them are AFGL 2591, AFGL 2136, AFGL 490, and S140 IRS 1 from the study of MIR sizes of Monnier et al. (2009), as well as W 33A (de Wit et al. 2007, 2010), and NGC 3603-IRS 9A (Vehoff et al. 2010). The sample of Herbig Be stars was also taken from Monnier et al. (2009). The disk size vs. luminosity diagram of these objects and NGC 2264 IRS 1, as well as the size vs. stellar mass diagram is shown in Fig. 7. Parameters such as stellar mass, distance, and the numbers for disk size and luminosity can be found in Table A.1. Both luminosity and mass of the central object seem to be correlated with the size of the MIR emission region. Owing to the factors considered above, objects with luminosities ranging between 1000 and 10,000 L_\odot display a large scatter in their sizes (a factor of around 10). The same is true for the mass range of $\sim 8 - 20 M_\odot$. The size of the MIR emitting region around NGC 2264 IRS 1 seems to be typical for their mass and luminosity.

4.2. Discussion of the radiative transfer models

Models of a circumstellar envelope only did not provide good fits, as they were unable to reproduce visibilities and NIR flux simultaneously. Furthermore, the estimated sizes of the dust distribution (Sect. 3.1) are different for different position angles, which implies that there is an asymmetric dust distribution.

The radiative transfer modeling performed with RADMC suggests that IRS 1 has an optical thick, but geometrically thin, flaring circumstellar disk with a mass of $0.1 M_\odot$. This is supported by the results of the SED fitting process using the Robitaille grid. Not only the best-fit Robitaille disk model but also the ten best-fit models have parameters describing the cen-

tral object and the circumstellar disk that compare very well with those of the best-fit model found using RADMC. However, the inclinations of the Robitaille models vary between 20° and 70° . The temperature and mass of the central object are slightly higher in all of these disk models than the values used for the RADMC model.

The two blackbody components producing the far-IR flux for our best-fit RADMC model could originate from a large surrounding cloud or envelope, respectively, that would with the large angular resolution of MIDI only be seen as foreground extinction. This would agree with the large foreground extinction (> 20 mag) as used in the best-fit RADMC and derived from the ten best-fit Robitaille disk models. Furthermore, previous publications have suggested that there is a large amount of foreground extinction with values between 20 mag (Thompson et al. 1998) and 35 mag (Thompson & Tokunaga 1978). The inclination of the best-fit RADMC model is 30° , but owing to the poor uv-coverage this value is poorly constrained. The position angle of the jet-like feature seen in the near-IR is 20° (see Fig. 8), and the position angle in our best-fit disk model is 40° . This does not match perfectly, but the value for the position angle is also poorly constrained. However, an overall geometric picture of a moderately inclined disk seems reasonable.

5. Summary & conclusions

We have presented MIDI mid-infrared interferometric observations of the massive young stellar object NGC 2264 IRS 1. The observed visibilities provide *no* hint of multiplicity of the central source in the separation range from ~ 30 AU (resolution limit) to ~ 230 AU (slit width limit). Geometric models (Sect. 3.1) suggest a size of $\sim 30 - 60$ AU for the mid-infrared emission region. This value is in good agreement with the mid-infrared sizes of similar objects.

Our modeling shows that a simple temperature-gradient model for a circumstellar disk can reproduce the SED at mid- and far-IR wavelengths, but fails to reproduce the SED in the near-IR and the observed visibilities; this model can therefore be ruled out.

We have performed a detailed radiative transfer modeling of the observed SED and visibilities with the RADMC code. It sug-

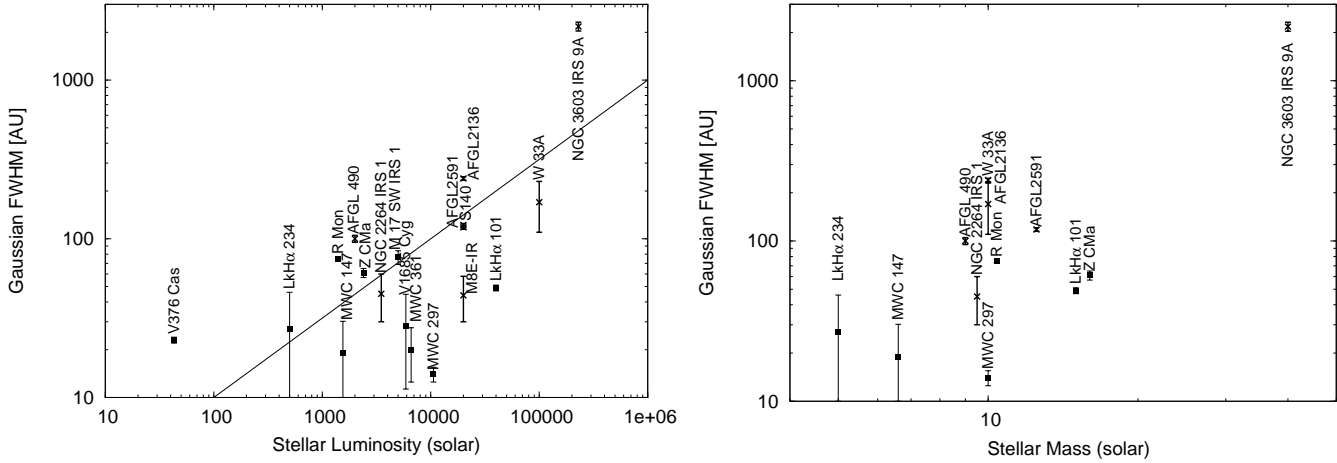


Fig. 7. *Left:* Mid-infrared-size-luminosity diagram. Rectangulars correspond to Herbig Be stars, crosses to MYSOs. Values and references are shown in Table A.1. The black line corresponds to a $R \propto \sqrt{L}$ relation. *Right:* Mid-infrared-size-stellar-mass diagram. Rectangulars correspond to Herbig Be stars, crosses to MYSOs.

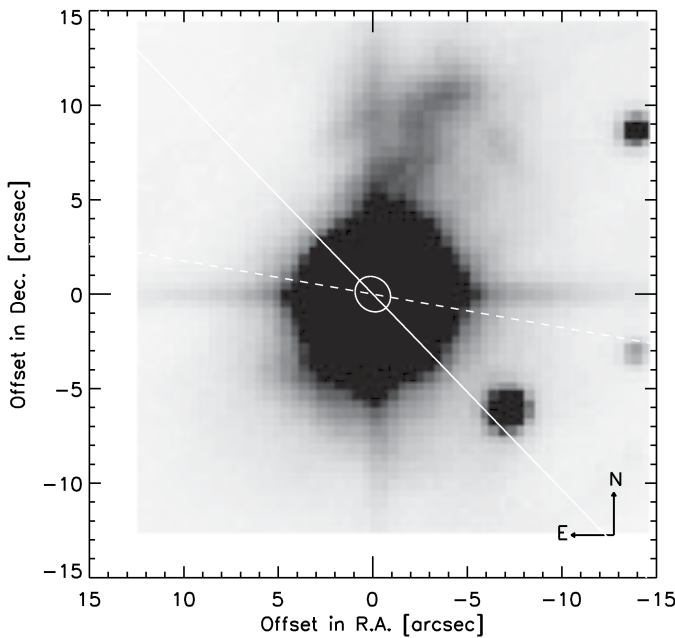


Fig. 8. K-band image of NGC 2264 IRS 1 from Schreyer et al. (1997). We overlay an ellipse (white) that shows a disk seen under an inclination of 30° and a position angle of 40° . The size of the disk is not drawn to scale. The solid white line shows the orientation of the 40 m baseline, the dashed one the orientation of the 90 m baseline.

gests a scenario of a geometrically flat but optically thick circumstellar dust disk. We also used the fitting tool by Robitaille et al. (2007), which leads to similar disk models and therefore confirms the results obtained with RADMC, whereas envelope models found within the Robitaille grid did not provide similarly good fits to SED and visibilities simultaneously. Although there is no observational evidence, the possible presence of a large ($r \geq 400$ AU) spherical envelope around the disk cannot be excluded by the data. The mass of the circumstellar disk is about $0.1 M_\odot$. The data suggest an inclination angle of $\sim 30^\circ$ and a position angle of $\sim 40^\circ$ for the orientation of the disk. These values are consistent with an overall geometrical model

based on the jet-like feature seen to the north-east of IRS 1. Comparing NGC 2264 IRS 1 to other YSOs, the size of its MIR emitting region seems to be typical of its luminosity and mass. However, the large scatter of sizes in this range of luminosities and masses points towards a wide variety of (disk) morphologies among these objects.

More observational research, such as future MIR interferometric observations, will provide tighter constraints on the circumstellar material around this interesting source and therefore will help us to clarify our understanding of the disks around high-mass YSOs.

Acknowledgements. We would like to thank the anonymous referee for his suggestions and comments that helped to improve the paper. We would also like to thank K. Dullemond for explanations and discussions about RADMC. We gratefully acknowledge funding of this work by the German *Deutsche Forschungsgemeinschaft*, DFG project number PR 569/8-1.

References

- Acke, B. & van den Ancker, M. E. 2004, A&A, 426, 151
- Acke, B., Verhoelst, T., van den Ancker, M. E., et al. 2008, A&A, 485, 209
- Allen, D. A. 1972, ApJ, 172, L55
- Alonso-Albi, T., Fuente, A., Bachiller, R., et al. 2009, A&A, 497, 117
- Baxter, E. J., Covey, K. R., Muench, A. A., et al. 2009, AJ, 138, 963
- Benisty, M., Natta, A., Isella, A., et al. 2010, A&A, 511, A74
- Berger, J. P. & Segransan, D. 2007, New A Rev., 51, 576
- Bonnell, I. A. & Bate, M. R. 2006, MNRAS, 370, 488
- Bonnell, I. A., Bate, M. R., & Zinnecker, H. 1998, MNRAS, 298, 93
- Cesaroni, R., Neri, R., Olmi, L., et al. 2005, A&A, 434, 1039
- Chiang, E. I. & Goldreich, P. 1997, ApJ, 490, 368
- Chini, R., Kruegel, E., & Kreysa, E. 1986, A&A, 167, 315
- Crampton, D. & Fisher, W. A. 1974, Publications of the Dominion Astrophysical Observatory Victoria, 14, 283
- Cunningham, A., Krumholz, M. R., Klein, R. I., & McKee, C. F. 2009, in American Astronomical Society Meeting Abstracts 214, 604.05
- de Wit, W. J., Hoare, M. G., Fujiyoshi, T., et al. 2009, A&A, 494, 157
- de Wit, W. J., Hoare, M. G., Oudmaijer, R. D., & Lumsden, S. L. 2010, A&A, 515, A45
- de Wit, W. J., Hoare, M. G., Oudmaijer, R. D., & Mottram, J. C. 2007, ApJ, 671, L169
- Draine, B. T. & Lee, H. M. 1984, ApJ, 285, 89
- Drew, J. E., Busfield, G., Hoare, M. G., et al. 1997, MNRAS, 286, 538
- Dullemond, C. P. & Dominik, C. 2004, A&A, 417, 159
- Follert, R., Linz, H., Stecklum, B., et al. 2010, A&A, 522, A17
- Fuente, A., Rizzo, J. R., Caselli, P., Bachiller, R., & Henkel, C. 2005, A&A, 433, 535

- Gibb, E. L., Whittet, D. C. B., Boogert, A. C. A., & Tielens, A. G. G. M. 2004, *ApJS*, 151, 35
- Guertler, J., Henning, T., Koempe, C., et al. 1996, *A&A*, 315, L189
- Harvey, P. M., Campbell, M. F., & Hoffmann, W. F. 1977, *ApJ*, 215, 151
- Herbig, G. H., Andrews, S. M., & Dahm, S. E. 2004, *AJ*, 128, 1233
- Herbst, E. & van Dishoeck, E. F. 2009, *ARA&A*, 47, 427
- Hernández, J., Calvet, N., Briceño, C., Hartmann, L., & Berlind, P. 2004, *AJ*, 127, 1682
- Kastner, J. H., Weintraub, D. A., & Aspin, C. 1992, *ApJ*, 389, 357
- Köhler, R. & Jaffe, W. 2008, in *The Power of Optical/IR Interferometry: Recent Scientific Results and 2nd Generation* (Springer, Heidelberg), ed. A. Richichi, F. Delplancke, F. Paresce, & A. Chelli, 569
- Kraus, S., Hofmann, K., Menten, K. M., et al. 2010, *Nature*, 466, 339
- Kraus, S., Preibisch, T., & Ohnaka, K. 2008, *ApJ*, 676, 490
- Kuiper, R., Klahr, H., Beuther, H., & Henning, T. 2010, *ApJ*, 722, 1556
- Leinert, C., Graser, U., Przygodda, F., et al. 2003, *Ap&SS*, 286, 73
- Leinert, C., van Boekel, R., Waters, L. B. F. M., et al. 2004, *A&A*, 423, 537
- Lester, D. F., Harvey, P. M., Joy, M., & Ellis, Jr., H. B. 1986, *ApJ*, 309, 80
- Linz, H., Henning, T., Feldt, M., et al. 2009, *A&A*, 505, 655
- Malbet, F., Lachaume, R., Berger, J., et al. 2005, *A&A*, 437, 627
- Mathis, J. S., Rumpl, W., & Nordsieck, K. H. 1977, *ApJ*, 217, 425
- McKee, C. F. & Tan, J. C. 2003, *ApJ*, 585, 850
- Men'shchikov, A. B. & Henning, T. 1997, *A&A*, 318, 879
- Monnier, J. D., Millan-Gabet, R., Billmeier, R., et al. 2005, *ApJ*, 624, 832
- Monnier, J. D., Tuthill, P. G., Ireland, M., et al. 2009, *ApJ*, 700, 491
- Murakawa, K. 2010, *A&A*, 522, A46
- Murakawa, K., Preibisch, T., Kraus, S., et al. 2008, *A&A*, 488, L75
- Nakano, M., Sugitani, K., & Morita, K. 2003, *PASJ*, 55, 1
- Osorio, M., Anglada, G., Lizano, S., & D'Alessio, P. 2009, *ApJ*, 694, 29
- Ratzka, T., Schegerer, A. A., Leinert, C., et al. 2009, *A&A*, 502, 623
- Robitaille, T. P., Whitney, B. A., Indebetouw, R., & Wood, K. 2007, *ApJS*, 169, 328
- Robitaille, T. P., Whitney, B. A., Indebetouw, R., Wood, K., & Denzmore, P. 2006, *ApJS*, 167, 256
- Sargent, A. I., van Duinen, R. J., Nordh, H. L., et al. 1984, *A&A*, 135, 377
- Schreyer, K., Helmich, F. P., van Dishoeck, E. F., & Henning, T. 1997, *A&A*, 326, 347
- Schreyer, K., Semenov, D., Henning, T., & Forbrich, J. 2006, *ApJ*, 637, L129
- Schreyer, K., Stecklum, B., Linz, H., & Henning, T. 2003, *ApJ*, 599, 335
- Schwartz, P. R., Thronson, Jr., H. A., Odenwald, S. F., et al. 1985, *ApJ*, 292, 231
- Shevchenko, V. S. & Yakubov, S. D. 1989, *Soviet Ast.*, 33, 370
- Sloan, G. C., Kraemer, K. E., Price, S. D., & Shipman, R. F. 2003, *ApJS*, 147, 379
- Thamm, E., Steinacker, J., & Henning, T. 1994, *A&A*, 287, 493
- Thiebaut, E., Bouvier, J., Blazit, A., et al. 1995, *A&A*, 303, 795
- Thompson, R. I., Corbin, M. R., Young, E., & Schneider, G. 1998, *ApJ*, 492, L177
- Thompson, R. I. & Tokunaga, A. T. 1978, *ApJ*, 226, 119
- Tristram, K. R. W. 2007, PhD thesis, Max-Planck-Institut für Astronomie (Heidelberg)
- van der Tak, F. F. S., van Dishoeck, E. F., Evans, II, N. J., Bakker, E. J., & Blake, G. A. 1999, *ApJ*, 522, 991
- Vehoff, S., Hummel, C. A., Monnier, J. D., et al. 2010, *A&A*, 520, A78
- Ward-Thompson, D., Zylka, R., Mezger, P. G., & Sievers, A. W. 2000, *A&A*, 355, 1122
- Whitney, B. A., Wood, K., Bjorkman, J. E., & Wolff, M. J. 2003, *ApJ*, 591, 1049
- Zinnecker, H. & Bate, M. R. 2002, in *Astronomical Society of the Pacific Conference Series*, Vol. 267, Hot Star Workshop III: The Earliest Phases of Massive Star Birth (ASP, San Francisco), ed. P. Crowther, 209
- Zinnecker, H. & Yorke, H. W. 2007, *ARA&A*, 45, 481

Appendix A: Parameters and references for size-luminosity plot

Table A.1. MIR-sizes of MYSOs and Herbig Be stars

Object	Diameter [AU]	Distance [pc]	Luminosity [L_\odot]	Mass [M_\odot]	SpT	Reference
NGC 3603 IRS 9A	2177	7000	$2.3 \cdot 10^5$	40		1
W 33A	115-230	3800	$1 \cdot 10^5$	10		2
V376 Cas	23	630	43		B5e	3, 4
MWC 147	19	800	1550	6.6	B6	3, 5, 6
R Mon	75	800	1400	10.4	B0	3, 7, 8
Z CMa	61	1000	2400	16	B	3, 9, 10
MWC 297	14	250	10600	10	B1.5	3, 11, 12
V1685 Cyg	28	980	5890		B3	3, 4
MWC 361	20	440	6600		B2	3, 4
LkH α 234	27	1000	500	5	B7	3, 13, 14
AFGL 490	100	1000	$2 \cdot 10^3$	8-10	B2	3, 15
LkH α 101	49	700	$2 \cdot 6 \cdot 10^4$	15	Be	3, 16
S140 IRS 1	122	910	$2 \cdot 10^4$			3, 17, 18
AFGL 2136	240	2000	$2 \cdot 10^4$	>10		3, 19
AFGL 2591	118	1000	$2 \cdot 10^4$	10-15		3, 20
M 17 SW IRS 1	69-84	2100	$5 \cdot 10^3$		B0	21
M8E-IR	30-57	1500	$2 \cdot 10^4$		B0	22
NGC 2264 IRS 1	30-60	913	$1.5 \cdot 4.7 \cdot 10^3$	9.5	B0-B2	see Chapt. 1, 3.1

References. (1) Vehoff et al. (2010); (2) de Wit et al. (2007); (3) Monnier et al. (2009); (4) Acke & van den Ancker (2004); (5) Kraus et al. (2008); (6) Hernández et al. (2004); (7) Murakawa et al. (2008); (8) Murakawa (2010); (9) Alonso-Albi et al. (2009); (10) Thiebaut et al. (1995); (11) Acke et al. (2008); (12) Drew et al. (1997); (13) Shevchenko & Yakubov (1989); (14) Fuente et al. (2005); (15) Schreyer et al. (2006); (16) Herbig et al. (2004); (17) Crampton & Fisher (1974); (18) Lester et al. (1986); (19) Kastner et al. (1992); (20) van der Tak et al. (1999); (21) Follert et al. (2010); (22) Linz et al. (2009).